Taylor & Francis
Taylor & Francis Group

Automatika

Journal for Control, Measurement, Electronics, Computing and Communications

ISSN: (Print) (Online) Journal homepage: www.tandfonline.com/journals/taut20

Stabilization control of rotary inverted pendulum using a novel EKF-based fuzzy adaptive sliding-mode controller: design and experimental validation

Omer Saleem, Turki Alsuwian, Arslan Ahmed Amin, Shehryaar Ali & Zuhair A. Alqarni

To cite this article: Omer Saleem, Turki Alsuwian, Arslan Ahmed Amin, Shehryaar Ali & Zuhair A. Alqarni (2024) Stabilization control of rotary inverted pendulum using a novel EKF-based fuzzy adaptive sliding-mode controller: design and experimental validation, Automatika, 65:2, 538-558, DOI: 10.1080/00051144.2024.2312309

To link to this article: https://doi.org/10.1080/00051144.2024.2312309

AUTOMATIKA
2024, VOL. 65, NO. 2, 538–558
https://doi.org/10.1080/00051144.2024.2312309

Stabilization control of rotary inverted pendulum using a novel EKF-based fuzzy adaptive sliding-mode controller: design and experimental validation

Omer Saleem[a], Turki Alsuwian[b], Arslan Ahmed Amin [c], Shehryaar Ali[d] and Zuhair A. Alqarni[e]

[a]Department of Electrical Engineering, FAST – National University of Computer and Emerging Sciences, Lahore, Pakistan; [b]Department of Electrical Engineering, College of Engineering, Najran University, Najran, Saudi Arabia; [c]Department of Electrical Engineering, FAST – National University of Computer and Emerging Sciences (NUCES), Chiniot, Pakistan; [d]School of Electrical Engineering and Computer Sciences, National University of Science and Technology (NUST), Islamabad, Pakistan; [e]Electrical Engineering Department, Al-Baha University, Al-Aqiq, Saudi Arabia

ABSTRACT

This article methodically develops an improved self-regulating fuzzy-adaptive Sliding Mode Controller (SMC) that strengthens the disturbance compensation capacity of the nonlinear rotary pendulum systems while effectively attenuating the chattering content and curbing the control energy consumption. The article contributes to augmenting the SMC with online adaptation tools to achieve the said objectives. It employs the conventional Gao's power-rate reaching law as the baseline. The scaling gain and the power rate of the said reaching law are adaptively modulated via a pre-calibrated two-input state-error-driven fuzzy nonlinear function. Additionally, the sign function in the law is also replaced with an odd-symmetric nonlinear fuzzy function to address the hard limits imposed by the former. Finally, the membership functions of the fuzzy function are self-regulated using the Extended-Kalman-Filter to improve the compensator's adaptability in handling the system's rapidly changing control requirements under exogenous disturbances. The aforementioned propositions are verified by performing customized and reliable hardware-in-loop experiments on the Quanser single-link rotary pendulum platform. As compared to baseline SMC law, the proposed control procedure contributes a ∼45.2%, ∼48.5%, and ∼34.8% reduction in position-regulation errors, control energy consumption, and peak overshoots, respectively. The experimental assessment validates the proposed control system's enhanced robustness and chattering-suppression capability.

ARTICLE HISTORY
Received 13 March 2023
Accepted 25 January 2024

KEYWORDS
Sliding-mode-control; fuzzy nonlinear function; Extended-Kalman-Filter; adaptive tuning; experimental validation

1. Introduction

Single-link Rotary-Inverted-Pendulum (RIP) is an under-actuated mechatronic platform that is widely favored in the domain of experimental physics and control systems engineering due to its complex geometry, multiple degrees of freedom, nonlinear dynamics, kinematic instability, and under-actuated configuration [1,2]. These properties make it a perfect experimental setup to test the agility and resilience of the nonlinear control law [3,4]. The stabilization control problem of the RIP becomes quite difficult to tackle under bounded exogenous disturbances and parametric uncertainties [5]. This challenging problem is evident in various practical scenarios, such as the stabilization of Segway platforms, the satellites in orbit, the attitude of underwater vessels, the gait of legged robots, the vertical take-off of helicopters and rotorcrafts, the building under structural vibrations (tremors or earthquakes), and the launching of rockets and missiles, etc [6,7].

1.1. Literature review

Several robust stabilization control strategies have been scientifically investigated for standard RIP systems [8–10]. Fixed-gain PID controllers are considered reliable in self-balancing robotic applications [11,12]. However, the simplicity of their structure prevents them from fully realizing and efficiently addressing nonlinear disturbances [13,14]. The fuzzy-logic controllers require a pre-calibrated set of fuzzy rules that are defined by the control expert [1,15]. Their membership functions (MFs) can be calibrated offline to eliminate any discrepancies in the heuristically established logical rules to formulate a robust fuzzy control law [16,17]. The neural controllers, despite their flexibility, require extensive training to deliver a reliable control effort, which inevitably affects their computational economy [18]. The dependence of the optimal state-feedback linear quadratic regulator (LQR) on the dynamic system's mathematical model affects the optimality of its control

CONTACT Arslan Ahmed Amin dr.arslanamin@gmail.com; arslan_engineer61@yahoo.com FAST – National University of Computer and Emerging Sciences (NUCES), Chiniot-Faisalabad Campus, Sargodha Road, Chiniot, Punjab, Pakistan

yield when the system encounters model uncertainties and identification errors in real time [19,20]. Extensive research has been done to improve the LQR's capability by augmenting it with auxiliary self-adaptation tools to effectively compensate for bounded exogenous disturbances [21–23].

The Sliding Mode Controller (SMC) is a widely favored nonlinear feedback compensator [21]. It delivers robust control effort and efficiently compensates for exogenous disturbances and parametric uncertainties that cannot be practically handled via the aforementioned control schemes otherwise [24,25]. It belongs to the class of variable structure control, wherein the control law commutes between the sliding manifolds using a pre-calibrated switching function to address the rapid state variations [26,27]. The SMC scheme and its variants have been extensively proposed in the available literature to develop an agile self-balancing control strategy for RIPs [28]. The sliding-mode control schemes offer robust disturbance rejection while guaranteeing finite-time convergence [29,30]. However, the SMC's redundant switching phenomenon generates highly disruptive control input, which inevitably injects chattering and ripples in the state response. This behavior leads to high oscillations of the RIP's mechanical parts as well as dynamic power losses in the reactive electrical devices [31,32]. Furthermore, it is required to effectively manipulate the control stiffness as per the state error variations to amplify the damping against disturbances and to increase the transient response speed while economizing the control energy and preserving stability.

The chattering effect is generally caused by any of the following three reasons: (1) the un-modeled intrinsic nonlinearities; (2) the ill-calibrated switching gain; and (3) the discontinuous switching function [33]. Some of the notable techniques devised to effectively minimize chattering are the adaptive SMC, DSMC, and Fuzzy SMC [34]. Filtering out the high-frequency noise components from the SMC's control signals has gained a lot of traction [35]. Replacing the conventional signum function with a fuzzy-logic inference mechanism to avoid the signum function's hard nonlinearity tends to improve the chattering suppression behavior [36]. However, to achieve the desired chattering suppression, these schemes tend to compromise the SMC's robustness and affect its adaptability against external perturbations [37]. Furthermore, the poor calibration of the fuzzy membership functions or the inaccuracies (caused by the expert's lack of knowledge) in the fuzzy logic rules incapacitate the fuzzy inference mechanism to yield robust and agile control effort under rapidly changing error conditions.

The disturbance-observer-based adaptive sliding mode controller designs have also been proposed in the scientific literature to counteract unknown disturbances actively [38,39]. The memory-based fuzzy systems and reinforcement learning-based adaptation strategies used in these works enhance the controller's robustness at the cost of higher computational complexity and, thus, higher computational burden on the embedded processing unit.

1.2. Main contributions

To address the aforementioned problems, this article presents the systematic formulation and performance validation of an innovative self-regulating fuzzy-adaptive SMC design for the RIP systems to minimize chattering while maintaining the agility of the SMC against under bounded disturbances. Gao's power-rate SMC procedure is used as the baseline reaching law, as expressed below [34].

$$u = -k|s(t)|^{\beta} f(s, \dot{s}) \tag{1}$$

where, k represents the preset positive scaling gain, $s(t)$ is the sliding surface that is computed as the weighted sum of all state errors, β is the preset power rate of the magnitude of $s(t)$, and $f(s, \dot{s})$ is an odd-symmetric fuzzy nonlinear function that is bounded between -1 and 1 as the state error conditions vary. This limiter function $f(s, \dot{s})$ avoids the hard nonlinearity of the $sign(s)$ function, and thus suppresses the chattering content in the state response(s). In this article, the aforementioned FSMC law is methodically evolved by augmenting it with a customized self-regulation block that improves its disturbance-rejection ability, economizes control expenditure, and attenuates the chattering in the response. The salient features of the proposed self-regulating SMC law are as follows:

(1) The power rate, β, and scaling gain, k, of the reaching law are adaptively modulated online via the pre-calibrated nonlinear fuzzy function$f(s, \dot{s})$ by using well-postulated meta-rules.
(2) The fuzzy MFs of the function $f(s, \dot{s})$ are self-regulated online via Extended Kalman Filter (EKF) to efficiently adapt to the abrupt changes in the state errors.
(3) The efficacy of the proposed scheme is investigated against the conventional SMC laws, in the physical environment, by conducting reliable and customized Hardware-In-Loop (HIL) experiments on the Quanser RIP.

The proposed FSMC law variant reinforces the compensator's dexterity to automatically regulate control stiffness as per the state error variations while (concurrently) attenuating the chattering content. The self-organizing fuzzy MFs aid in removing any shortcomings or residual inaccuracies in the heuristically defined rule base due to the imprecise knowledge of the expert. Furthermore, it reconfigures the waveform of the fuzzy function in real time to accurately alter the relevant

controller gains to address the system's requirements. Consequently, the proposed SMC law increases the response speed, strengthens the system's immunity against disturbances, improves chattering suppression behavior, and preserves the control economy by avoiding peak servo requirements.

The idea of employing an EKF-based self-regulating nonlinear fuzzy function to adaptively modulate the odd limiter function, power rate, and scaling gain of the SMC reaching law to simultaneously enhance the disturbance-rejection and chattering attenuation capability has not been investigated in the open literature. Hence, this novel idea is the main focus of this article.

The article is structured as follows: The dynamic model and the baseline SMC law for the RIP system are presented in Section 2. The FSMC law augmented with online adaptive parameters is derived in Section 3. The proposed EKF-based self-regulation fuzzy adaptive SMC law is formulated in Section 4. Section 5 presents the comparative experimental analysis of the designed SMC variants. Finally, Section 6 concludes the article.

2. System description

The proposed SMC law is validated by benchmarking its performance using the standard single-link RIP system. The single-link RIP system is diagrammatically illustrated in Figure 1. It has a stable and unstable equilibrium state. The rod is vertically downright in the stable state, whereas the rod is balanced vertically upright in the unstable state. Thus, an active balancing control effort is required to maintain the rod in the equilibrium state. The arm of the RIP system is rotated by mounting it on the DC servo motor's shaft. The motor's shaft is equipped with a rotary encoder that records the arm's position α in real-time. The pendulum's rod is attached to the other end of the arm via a hinge that is instrumented with another rotary encoder that records the apparatus's rod position θ. The data acquired from each encoder is transmitted to the control software application over a serial link. The software application processes the data to compute the control command. The resulting motor control torque rotates the pendulum arm, which continuously provides the necessary swinging energy to the rod to invert it and eventually balance it.

2.1. Mathematical model derivation

The single-link RIP system is modeled in terms of α and θ via the Euler–Lagrange method [40]. The computation of RIP's Lagrangian, L, is presented in Eq. 2.

$$L = E_K - E_P \tag{2}$$

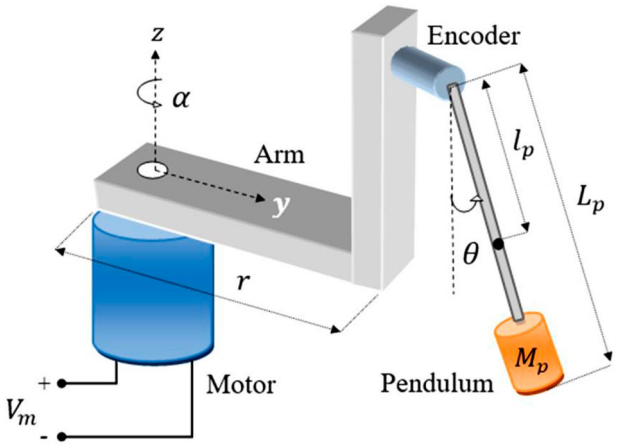

Figure 1. Schematic diagram of a single-link RIP system.

where $E_P = M_p l_p g(\cos\theta)$, and $E_K = \frac{1}{2}J_e(\dot{\alpha})^2 + \frac{1}{2}M_p(r\dot{\alpha} - l_p\dot{\theta}(\cos\theta))^2 + \frac{1}{2}M_p(-l_p\dot{\theta}(\sin\theta))^2 + \frac{1}{2}J_p(\dot{\theta})^2$ where E_K and E_P represent the RIP's total kinetic and total potential energy, respectively. The parameters mentioned in the above expressions are quantified in Table 1. The computed Lagrangian is expressed as follows [36].

$$L = \frac{1}{2}(J_e + M_p r^2)(\dot{\alpha})^2 + \left(\frac{2}{3}M_p {l_p}^2 + \frac{1}{2}J_p\right)(\dot{\theta})^2 - M_p l_p r(\cos\theta)\dot{\alpha}\dot{\theta} - M_p l_p g(\cos\theta) \tag{3}$$

The nonlinear equations of motion are derived by evaluating the following partial derivatives [40].

$$\frac{\delta}{\delta t}\left(\frac{\delta L}{\delta \dot{\alpha}}\right) - \frac{\delta L}{\delta \alpha} = \tau, \frac{\delta}{\delta t}\left(\frac{\delta L}{\delta \dot{\theta}}\right) - \frac{\delta L}{\delta \theta} = 0 \tag{4}$$

where τ represents the torque applied by DC motor. It is a function of the motor's terminal voltage, V_m, as shown below.

$$\tau = \frac{K_t(V_m - K_m\dot{\alpha})}{R_m} \tag{5}$$

After linearization, the following state equations are obtained.

$$\ddot{\alpha}(t) = \frac{1}{H}\left(rM_p^2 l_p^2 g\theta(t) - \frac{(J_p + M_p l_p^2)K_t K_m}{R_m}\dot{\alpha}(t) + \frac{(J_p + M_p l_p^2)K_t}{R_m}V_m(t)\right) \tag{6}$$

$$\ddot{\theta}(t) = \frac{1}{H}\left(M_p l_p g(J_e + M_p r^2)\theta(t) - \frac{rM_p l_p K_t K_m}{R_m}\dot{\alpha}(t) + \frac{rM_p l_p K_t}{R_m}V_m(t)\right) \tag{7}$$

such that, $H = J_e J_p + M_p r^2 J_p + M_p l_p^2 J_e$

The generalized state-space representation of a linear dynamical system is shown in Eq. 7.

$$\dot{x}(t) = \boldsymbol{A}x(t) + \boldsymbol{B}u(t), y(t) = \boldsymbol{C}x(t) + \boldsymbol{D}u(t) \tag{8}$$

Table 1. Identification of the Quanser RIP Model Parameters [41].

Parameter	Designation	Value	Units
M_p	Pendulum's mass	0.027	kg
l_p	Pendulum's center of mass	0.153	m
L_p	Pendulum rod's length	0.191	m
r	Horizontal arm's length	0.083	m
M_{arm}	Arm's mass	0.028	kg
g	Gravitational acceleration	9.81	m/s^2
J_e	Motor shaft's moment	1.23×10^{-4}	kgm^2
J_p	Pendulum rod's moment	1.10×10^{-4}	kgm^2
R_m	Motor resistance	3.30	Ω
L_m	Motor inductance	47.0	mH
K_t	Motor torque constant	0.028	Nm/A
K_m	Back emf constant	0.028	V/(rad/s)
T_m	Maximum torque	0.14	Nm

where $\boldsymbol{A}$ is the system matrix, $\boldsymbol{B}$ is the input matrix, $\boldsymbol{C}$ is the output matrix, $\boldsymbol{D}$ is the feed-forward matrix, and $y(t)$ is the output vector. The state vector $x(t)$ and the control input vector $u(t)$ of the proposed system are presented in Eq. 8.

$$x(t) = \begin{bmatrix} \alpha(t) & \theta(t) & \dot{\alpha}(t) & \dot{\theta}(t) \end{bmatrix}^T,$$
$$u(t) = V_m(t) \tag{9}$$

The RIP system's model is represented in state-space form as shown below [36].

$$A = \begin{bmatrix} 0 & 0 & 1 & 0 \\ 0 & 0 & 0 & 1 \\ 0 & a_1 & a_2 & 0 \\ 0 & a_3 & a_4 & 0 \end{bmatrix}, B = \begin{bmatrix} 0 \\ 0 \\ b_1 \\ b_2 \end{bmatrix},$$
$$C = \begin{bmatrix} 1 & 0 & 0 & 0 \\ 0 & 1 & 0 & 0 \\ 0 & 0 & 1 & 0 \\ 0 & 0 & 0 & 1 \end{bmatrix}, D = \begin{bmatrix} 0 \\ 0 \\ 0 \\ 0 \end{bmatrix} \tag{10}$$

where,

$$a_1 = \frac{rM_p^2 l_p^2 g}{J_p J_e + J_e l_p^2 M_p + J_p M_p r^2},$$
$$a_2 = \frac{-K_t K_m (J_p + M_p l_p^2)}{(J_p J_e + J_e l_p^2 M_p + J_p M_p r^2) R_m},$$
$$a_3 = \frac{M_p l_p g (J_e + M_p r^2)}{J_p J_e + J_e l_p^2 M_p + J_p M_p r^2},$$
$$a_4 = \frac{-r M_p l_p K_t K_m}{(J_p J_e + J_e l_p^2 M_p + J_p M_p r^2) R_m},$$
$$b_1 = \frac{K_t (J_p + M_p l_p^2)}{(J_p J_e + J_e l_p^2 M_p + J_p M_p r^2) R_m},$$
$$b_2 = \frac{r M_p l_p K_t}{(J_p J_e + J_e l_p^2 M_p + J_p M_p r^2) R_m}$$

As mentioned earlier, the model parameters associated with Quanser RIP are quantified in Table 1 [41].

2.2. Baseline SMC law

The SMC law functions by driving the state trajectories of the RIP system toward a sliding surface, $s(t)$. The sliding surface utilized in this article is shown in Eq. 11.

$$s(t) = \boldsymbol{G}^T \varepsilon(t) \tag{11}$$

where, $\varepsilon(t) = x(t) - x_{ref}$

where $\boldsymbol{G}^T$ is a 1×4 vector containing the state error weights and x_{ref} represents the RIP system's reference state vector of the form $x_{ref} = \begin{bmatrix} \alpha_{ref} & \pi & 0 & 0 \end{bmatrix}^T$. The arm's initial position is set as its reference position, α_{ref}, before the beginning of every experiment. Owing to its rapid convergence, Gao's reaching law is used in this article [42]. The said reaching law is expressed in Eq. 12.

$$\dot{s}(t) = -k|s(t)|^{\beta} sign(s) \tag{12}$$

where k is the preset positive scaling gain, $\beta$is the preset power rate of the absolute value of $s(t)$ that is restricted between 0 and 1, and $sign(.)$ is a "sign" (or signum) function that is expressed in Eq. 13.

$$sign(s) = \begin{cases} 1, & \text{if } s(t) > 0 \\ 0, & \text{if } s(t) = 0 \\ -1, & \text{if } s(t) < 0 \end{cases} \tag{13}$$

The reaching law guarantees the convergence of the sliding surface $s(t)$ in finite time, as proven later in this section. The proposed finite-time SMC law is not required to address the variable time delays, as observed in bilateral teleoperators and similar nonlinear systems [30]. Hence, the said control law is formulated via a single term of exponential and limiter function to tackle the single sliding variable associated with the RIP system. This arrangement significantly simplifies the computational realization of the control structure. The first derivative of Eq. 11 is expressed in Eq. 14.

$$\dot{s}(t) = \boldsymbol{G}^T \dot{\varepsilon}(t) \tag{14}$$

where, $\dot{\varepsilon}(t) = \dot{x}(t) - \dot{x}_{ref}$

The expressions $\dot{x}_{ref} = \begin{bmatrix} 0 & 0 & 0 & 0 \end{bmatrix}^T$ and $\dot{x}(t) = \boldsymbol{A}x(t) + \boldsymbol{B}u(t)$, when substituted in Eq. 14, yield,

$$\dot{s}(t) = \boldsymbol{G}^T \boldsymbol{A} x(t) + \boldsymbol{G}^T \boldsymbol{B} u(t) \tag{15}$$

The comparison of Eq. 12 and Eq. 15 delivers the expression in Eq. 16.

$$-k|s(t)|^{\beta} sign(s) = \boldsymbol{G}^T \boldsymbol{A} x(t) + G^T \boldsymbol{B} u(t) \tag{16}$$

By making $u(t)$ as the subject, the state-space-driven SMC law is derived as shown below.

$$u(t) = -(\boldsymbol{G}^T \boldsymbol{B})^{-1} (\boldsymbol{G}^T \boldsymbol{A} x(t) + k|s(t)|^{\beta} sign(s)) \tag{17}$$

The stability of the SMC law is verified by using the positive-definite Lyapunov function in Eq. 18.

$$V(t) = 0.5(s(t))^2 \tag{18}$$

The first derivative of $V(t)$ is derived in Eq. 19.

$$\dot{V}(t) = s(t)\dot{s}(t) \tag{19}$$

Substituting the $\dot{s}(t)$ expression from Eq. 15, the derivative $\dot{V}(t)$ is expressed as shown in Eq. 20.

$$\dot{V}(t) = s(t)(\boldsymbol{G}^T\boldsymbol{A}x(t) + \boldsymbol{G}^T\boldsymbol{B}u(t)) \tag{20}$$

Substituting the $u(t)$ expression from Eq. 17, the derivative $\dot{V}(t)$ is simplified as shown below.

$$\begin{aligned}\dot{V}(t) &= s(t)(\boldsymbol{G}^T\boldsymbol{A}x(t) + (\boldsymbol{G}^T\boldsymbol{B})(-(\boldsymbol{G}^T\boldsymbol{B})^{-1}\\ &\quad (\boldsymbol{G}^T\boldsymbol{A}x(t) + k|s(t)|^{\beta}sign(s))))\\ &= s(t)(\boldsymbol{G}^T\boldsymbol{A}x(t) - (\boldsymbol{G}^T\boldsymbol{A}x(t) + k|s(t)|^{\beta}sign(s)))\\ &= s(t)(\boldsymbol{G}^T\boldsymbol{A}x(t) - \boldsymbol{G}^T\boldsymbol{A}x(t) - k|s(t)|^{\beta}sign(s))\\ &= s(t)(-k|s(t)|^{\beta}sign(s))\end{aligned} \tag{21}$$

The derivative function $\dot{V}(t)$ is simplified as shown in Eq. 22.

$$\dot{V}(t) = -k|s(t)|^{\beta+1} \tag{22}$$

Hence the expression of $\dot{V}(t) < 0$ if $k > 0$. This specification satisfies the stability requirements of the SMC law. The SMC law's finite-time convergence is analyzed as per Lemma 1 discussed below.

Lemma 2.1 ([29]): *Consider a positive-definite (continuous) function $z(t)$ that satisfies the differential inequality in Eq. 23, for $t > 0$.*

$$\dot{z}(t) \leq -\delta(z(t))^{\mu} \tag{23}$$

where δ and μ are predetermined constants such that $\delta > 0$ and $0 < \mu < 1$. The function $z(t)$ takes a finite time t_s to converge to zero. The time t_s is given in Eq. 24.

$$t_s \leq \frac{(z(0))^{1-\mu}}{\delta(1-\mu)} \tag{24}$$

Using the expression in Eq. 22, the derivative $\dot{V}(t)$ can be rewritten as shown in Eq. 25.

$$\dot{V}(t) = -\left(k(2)^{\frac{\beta+1}{2}}\right)(V(t))^{\frac{\beta+1}{2}} \tag{25}$$

Then, according to Lemma 1, the function $V(t)$ and the sliding variable $s(t)$ converge in a finite time that is given by Eq. 26, as long as $k > 0$ and $0 < \beta < 1$.

$$t_s \leq \frac{(V(0))^{\frac{1-\beta}{2}}}{\left(k(2)^{\frac{\beta+1}{2}}\right)\left(\frac{1-\beta}{2}\right)} \tag{26}$$

To ensure accurate position-regulation behavior, the SMC parameters are optimized by iteratively minimizing the following objective function J_c.

$$J_c = \int_0^{\infty} [|e_{\alpha}(t)|^2 + |e_{\theta}(t)|^2 + |u(t)|^2]dt \tag{27}$$

In this cost function, an equal (unity) weight is allocated to the state error and the control criteria. This is done to apply equal impact on minimization of the position regulation errors and the control input to prevent wind-up. The selection range of each coefficient of $\boldsymbol{G}^T$ is bounded within $[-100, 100]$. The parameter optimization is initialized with $\boldsymbol{G}^T = \begin{bmatrix}1 & 1 & 1 & 1\end{bmatrix}$. The tuning algorithm explores the range space for the best-fit solution in the direction of the objective function's decreasing gradient. In every trial, the RIP apparatus rod is inverted and balanced for 10.0 s. The corresponding cost is computed at the trial's conclusion. The optimization process is concluded when the global minimum is acquired for a given parameter. The parameters β and k are also tuned offline by using the aforementioned technique. The power rate β is bounded within [0, 1] and the scaling gain k is chosen from the range [0, 10] as discussed in Eq. 10. The tuning algorithm is initialized with $\beta = 1$ and $k = 1$. The parameter values thus selected are $k = 4.07$, $\beta = 0.45$, and $\boldsymbol{G}^T = \begin{bmatrix}-3.16 & 73.48 & -3.02 & 9.25\end{bmatrix}$, (See [40]).

The utilization of linear models for control design is preferred over nonlinear models primarily due to their simplicity and tractability. The linear differential equations are computationally simpler to solve, which leads to easier analysis, design, and realization of the control laws. Furthermore, it is also much simpler to assess the stability and robustness of a control design without having to simulate the entire nonlinear system. The computational efficiency of linear systems is especially important in real-time applications that require quick response speeds. The control designers can focus on the behavior of the system near specific operating points by linearizing the nonlinear systems to create linear models. This streamlines the design process and is adequate for a variety of applications. Hence, owing to the aforementioned benefits, the SMC law expressed in Eq. 17 uses the system's linear state space model. This arrangement also increases the scalability of the SMC. The intrinsic nonlinear properties of the underactuated systems are difficult to model and identify owing to their complex geometry.

The SMC discussed in this work is formulated using a linear state space model. Despite working with a linear system model, the proposed SMC law is augmented with auxiliary online adaptation tools that are realized using model-free nonlinear fuzzy functions. These functions autonomously self-tune the critical parameters as the error conditions vary, which aids in amplifying the controller's resilience against exogenous perturbations. This arrangement allows the designer to easily

modify and extend the SMC law to other mechatronic systems, as long as the linearized state space model is known a priori.

2.3. Baseline linear control law

The conventional LQR is a state space compensator that minimizes the QCF provided in Eq. 28 to provide optimal control decisions [19,20].

$$J_{lq} = \frac{1}{2}\int_0^\infty [u(t)^T \boldsymbol{R} u(t) + x(t)^T \boldsymbol{Q} x(t)]dt \tag{28}$$

where $\boldsymbol{R} \in \mathbb{R} \geq 0$ is the control input weighting factor and $\boldsymbol{Q} \in \mathbb{R}^{4\times4} > 0$ is the state weighting matrix linked with the single-link RIP system. The $\boldsymbol{R}$ and $\boldsymbol{Q}$ matrices are expressed in Eq. 29.

$$\boldsymbol{R} = \rho, \boldsymbol{Q} = \text{diag}\begin{pmatrix} q_\varphi & q_\theta & q_{\dot\alpha} & q_{\dot\theta} \end{pmatrix} \tag{29}$$

where ρ and q_x are the preset positive coefficients of the respective matrices. These coefficients are calibrated offline by minimizing the objective function in Eq. 27 using the procedure discussed in 2.2. The Algebraic-Riccati-Equation (ARE) uses the pre-calibrated $\boldsymbol{R}$ and $\boldsymbol{Q}$ matrices to evaluate $\boldsymbol{P}$ matrix as expressed in Eq. 30.

$$\boldsymbol{A}^T\boldsymbol{P} + \boldsymbol{P}\boldsymbol{A} - \boldsymbol{P}\boldsymbol{B}\boldsymbol{R}^{-1}\boldsymbol{B}^T\boldsymbol{P} + \boldsymbol{Q} = 0 \tag{30}$$

where $\boldsymbol{P} \in \mathbb{R}^{4\times4} > 0$. The corresponding LQR gain vector $\boldsymbol{K}$ is computed as expressed in Eq. 31.

$$\boldsymbol{K} = \boldsymbol{R}^{-1}\boldsymbol{B}^T\boldsymbol{P} \tag{31}$$

where $\boldsymbol{K} = \begin{bmatrix} k_\varphi & k_\theta & k_{\dot\alpha} & k_{\dot\theta} \end{bmatrix}$. The fixed-gain LQR law is formulated in Eq. 32.

$$u(t) = -\boldsymbol{K}x(t) \tag{32}$$

The closed-loop asymptotic stability of LQR is verified via the following Lyapunov function [21,22].

$$M(t) = x(t)^T\boldsymbol{P}x(t) > 0, \qquad \text{for } x(t) \neq 0 \tag{33}$$

The first derivative of $M(t)$ is derived in Eq. 34.

$$\begin{aligned} \dot M(t) &= 2x(t)^T\boldsymbol{P}\dot x(t) \\ &= 2x(t)^T\boldsymbol{P}(\boldsymbol{A} - \boldsymbol{B}\boldsymbol{K})x(t) \\ &= 2x(t)^T\boldsymbol{P}(\boldsymbol{A} - \boldsymbol{B}\boldsymbol{R}^{-1}\boldsymbol{B}^T\boldsymbol{P})x(t) \\ &= x(t)^T(\boldsymbol{P}\boldsymbol{A} + \boldsymbol{A}^T\boldsymbol{P})x(t) \\ &\quad - 2x(t)^T(\boldsymbol{P}\boldsymbol{B}\boldsymbol{R}^{-1}\boldsymbol{B}^T\boldsymbol{P})x(t) \end{aligned} \tag{34}$$

By making necessary substitutions from Eq. 25, $\dot V(t)$ simplified as expressed in Eq. 35.

$$\dot M(t) = -x(t)^T\boldsymbol{Q}x(t) - x(t)^T(\boldsymbol{P}\boldsymbol{B}\boldsymbol{R}^{-1}\boldsymbol{B}^T\boldsymbol{P})x(t) \tag{35}$$

The function $\dot M(t) < 0$ if $\boldsymbol{R} = \boldsymbol{R}^T > 0$ and $\boldsymbol{Q} = \boldsymbol{Q}^T \geq 0$. These conditions sufficiently prove the asymptotic stability of LQR. Based on the aforementioned stability specifications and the tuning technique discussed in Section 2.2, the weighting matrices of QCF are chosen by minimizing Eq. 27. The selected matrices are $\boldsymbol{R} = 1$ and $\boldsymbol{Q} = \text{diag}\begin{pmatrix} 38.2 & 52.6 & 5.3 & 2.1 \end{pmatrix}$. The LQR gains thus evaluated are $\boldsymbol{K} = \begin{bmatrix} -6.21 & 130.56 & -4.22 & 17.83 \end{bmatrix}$.

3. Fuzzy-Adaptive SMC methodology

The utilization of $sign(s)$ in Eq. 17 imposes a hard nonlinearity that induces abrupt switching in the generated control signals as the state errors vary. The repetitive switching causes highly disrupted control behavior that unavoidably contributes to chattering in the response. To minimize the chattering, the $sign(s)$ in Eq. 17 is replaced with a smooth fuzzy nonlinear function [43]. The function $f(s,\dot s)$ smoothly commutes between the sliding surfaces as an odd-symmetric function of s and $\dot s$. It is designed such that it is bounded between -1 and 1 so that it complies with the control law requirements. It uses s and $\dot s$ as its inputs, which improves the agility of the controller design to better address nonlinear disturbances. To further enhance agility and resilience, the SMC law is also retrofitted with online gain modulators that self-tune the controller's scaling gain and the power rate. By retrofitting the SMC control law with the aforementioned tools, the resulting Fuzzy Adaptive SMC law (or FA-SMC) takes the following form.

$$u_f(t) = -(\boldsymbol{G}^T\boldsymbol{B})^{-1}(\boldsymbol{G}^T\boldsymbol{A}x(t) + k(s,\dot s)|s(t)|^{\beta(s,\dot s)}f(s,\dot s)) \tag{36}$$

where $\beta(s,\dot s)$ and $k(s,\dot s)$ represent the time-varying power rate and scaling gain of the control law that is realized by using the aforesaid fuzzy function $f(s,\dot s)$. These modifications enhance the SMC's adaptability to efficiently compensate for the disturbance while attenuating the chattering phenomenon and maintaining smooth control activity. This scheme is computationally economical because it uses the prescribed $f(s,\dot s)$ to online adapt $k(.)$ and $\beta(.)$ instead of formulating a new gain-adaptation function. This control procedure is referred to as FA-SMC in this article. Its methodical construction is discussed below.

3.1. Fuzzy function formulation

The fuzzy-logic inference system is a computational intelligence paradigm that uses predefined qualitative rules to make logical decisions for solving problems in engineering cybernetics [44]. It utilizes heuristically fabricated logical rules to yield an agile control effort that undertakes to reject bounded external disturbances. The rules of $f(s,\dot s)$ are empirically designed to ensure the state trajectories always converge to the

Table 2. Rule base of the fuzzy function.

$f(s,\dot{s})$	$\dot{s}$						
s	NB	NM	NS	Z	PS	PM	PB
NB	NB	NB	NB	NM	NS	Z	Z
NM	NB	NB	NB	NS	Z	Z	PS
NS	NB	NB	NM	Z	Z	PS	PM
Z	NB	NM	NS	Z	PS	PM	PB
PS	NM	NS	Z	Z	PM	PB	PB
PM	NS	Z	Z	PS	PB	PB	PB
PB	Z	Z	PS	PM	PB	PB	PB

switching surface. The input and output states are linguistically defined via seven variables: namely, Negative Big (NB), Negative Medium (NM), Negative Small (NS), Zero (Z), Positive Small (PS), Positive Medium (PM), and Positive Big (PB). While defining the MFs, the variation in the inputs s and $\dot{s}$ are normalized within $[-1, 1]$. The fuzzy rules are synthesized as per the rationale discussed below:

(1) When both $s(t)$ and $\dot{s}(t)$ have the same polarities, the response is considered to be in the perturbed state. The fuzzy system applies a tight control effort to reject the disturbances during this phase.
(2) When $s(t)$ and $\dot{s}(t)$ have opposite polarities, the response is considered to be in the equilibrium or quasi-equilibrium state. The fuzzy system applies a soft control effort during this phase to minimize the state fluctuations as the response settles to the reference position.

These rules preserve the robustness of the conventional SMC law while suppressing the chattering content. The rule base synthesized to constitute $f(s,\dot{s})$ is presented in Table 2. The Mamdani inference method is used to implement the fuzzy implication, as shown below.

$$\mu_{ij} = \min(h_{i1}(s), h_{j2}(\dot{s})) \tag{37}$$

where μ represents the MF degree, n represents the rule number, and $h_{ij}(.)$ represents the triangular-shaped input MF as formulated in Eq. 38.

$$h_{ij}(g) = \begin{cases} 1 + \frac{g - c_{ij}}{b_{i,j}^{-}}, & -b_{ij}^{-} \le g - c_{ij} \le 0 \\ 1 - \frac{g - c_{ij}}{b_{ij}^{+}}, & 0 \le g - c_{ij} \le b_{ij}^{+} \\ 0, & \text{otherwise} \end{cases} \tag{38}$$

where g represents the normalized value of inputs (s or $\dot{s}$), and b_{ij}^{-}, c_{ij}, and b_{ij}^{+} are the left-half width, centroid, and right-half width of the j^{th} input MF of the i^{th} input respectively.

The decisions are defuzzified using the center of gravity approach, and the associated crisp output $f(s,\dot{s})$ is computed as shown in Eq. 39.

$$f(s,\dot{s}) = \frac{\sum_{i=1}^{7}\sum_{j=1}^{7}(\mu_{ij} \times w_{ij})}{\sum_{i=1}^{7}\sum_{j=1}^{7}\mu_{ij}} \tag{39}$$

where w is the output MF's centroid. Asymmetrical waveforms of the MFs are utilized in this work to strengthen the fuzzy-augmented SMC's robustness against exogenous perturbations. The fuzzy MFs are empirically optimized by utilizing the tuning procedure discussed in Section 2.2. The resulting triangular-shaped MFs linked with input and output variables are depicted in Figure 2. The execution of the fuzzy inference scheme does not involve any recursive computations, and thus, it can be easily programmed with modern embedded microprocessors.

3.2. Power rate adaptation

The power rate β of the reaching law influences the stiffness of control activity. A fixed β cannot address the ever-changing control requirements of the system. On the one hand, it yields insufficient control resources under disturbance conditions. Conversely, it applies surplus control energy during the equilibrium state. This arrangement renders the SMC law wasteful. Hence, in this article, β is dynamically reconfigured as a nonlinear scaling function of s and $\dot{s}$ that uses the following meta-rules.

(1) The power rate is decreased under large state-error conditions (disturbances). This helps in amplifying the influence of $|s(t)|^{\beta(s,\dot{s})}$ in the control law, thus applying an aggressive damping control force to attenuate the overshoots resulting from exogenous disturbances.
(2) The power rate is enlarged under small state-error conditions (equilibrium). This helps in reducing the influence of $|s(t)|^{\beta(s,\dot{s})}$ in the control law, thus applying a gentle control force to allow for smooth stabilization behavior around the equilibrium.

This rationale improves the disturbance attenuation of the system while preventing large servo requirements, thus maintaining a low chattering content in the response. The following nonlinear function is thus formulated in this work as per the aforementioned rationale.

$$\beta(s,\dot{s}) = 1 - (f(s,\dot{s}))^2 \tag{40}$$

where $\beta(s,\dot{s})$ represents the time-varying power rate. The power rate is self-adjusted between 0 and 1.

3.3. Scaling gain adaptation

Similar to the power rate, the scaling gain also directly manipulates the magnitude of the applied control force. A fixed scaling gain lacks the flexibility to address the abruptly varying control requirements as the operating conditions change. To robustify the system, the scaling gain is also adaptively modulated by using the following meta-rules.

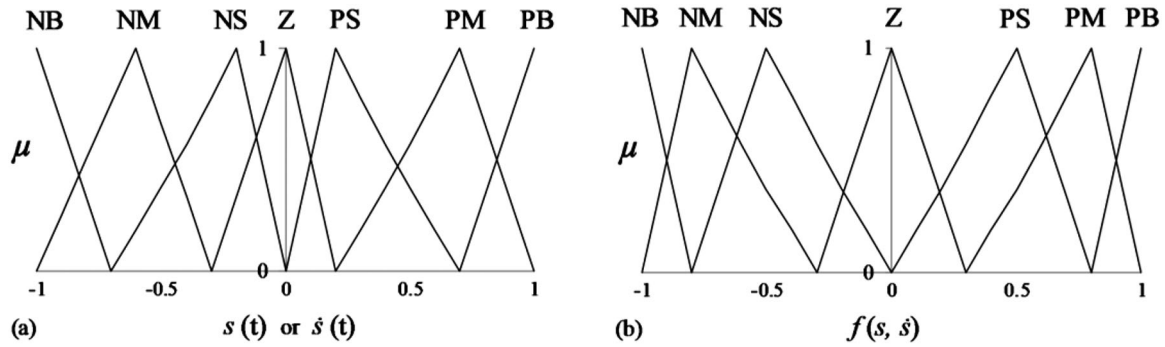

Figure 2. MFs linked with (a) input variables, and (b) output variables.

(1) The scaling gain is enlarged under large state errors to amplify the damping control force.
(2) The scaling gain is decreased under small state errors to soften the applied control force.

As per the aforementioned rules, the following smooth adaptation function is formulated.

$$k(s,\dot{s}) = k_o(f(s,\dot{s}))^2 \tag{41}$$

where $k(s,\dot{s})$ represents the time-varying scaling gain, and k_o is the nominal value of the scaling gain that is calibrated offline and set at $k_o = 6.84$ by using the tuning procedure prescribed in Section 2.2.

4. Self-Regulating fuzzy-adaptive SMC methodology

The EKF is a well-established state estimation and filtering technique that adapts to real-time changes in system dynamics [15]. If the system undergoes variations or if the model parameters change, the EKF will update the state estimate and covariance accordingly, leading to "self-regulating" behavior [46]. Hence, its adaptability to changing dynamics to yield real-time updates in the target parameters makes it well-suited for the proposed application. In this article, the EKF is used to adapt the output MFs of the function $f(s,\dot{s})$ [15]. Hence, the weights (w) and centers of the MF are probabilistically modified. The proposed fuzzy function uses the updated estimates of the said weights (w) and centers of the MF to reconfigure the shape of MF waveforms online. The updated MFs are used to re-compute the controller parameters of the SMC law after every sampling interval [45]. Consider the nonlinear system in Eq. 42.

$$q_{n+1} = m(q_n) + g_n, \quad d_n = p(q_n) + v_n \tag{42}$$

where, q_n represents the state vector of the system at n^{th} instance, g_n represents process noise, d_n represents observation vector, $p(.)$ is a nonlinear state function, and v_n represents observation noise. To reform the shape of output MFs online, the system's state vector is comprised of the left-half width, centroid, and right-half width of j^{th} input MF of i^{th} input, respectively [15].

$$q_n = [b_{11}{}^{-} c_{11} b_{11}{}^{+} \ldots b_{12}{}^{-} c_{12} b_{12}{}^{+} \ldots b_{72}{}^{-} c_{72} b_{72}{}^{+} w_{11} \ldots w_{77}] \tag{43}$$

The EKF is realized with the aid of the following set of equations.

$$F_n = I \tag{44}$$

$$H_n = \frac{\partial h(q_n)}{\partial q_n} = \frac{\partial m}{\partial q_n} = \left[\frac{\partial m}{\partial b_{11}{}^{-}} \frac{\partial m}{\partial c_{11}} \frac{\partial m}{\partial b_{11}{}^{+}} \cdots \frac{\partial m}{\partial w_{77}}\right] \tag{45}$$

$$P_{n+1} = P_n - K_n H_n P_n + M_n \tag{46}$$

$$K_n = P_n H_n{}^{T} (R_n + H_n P_n H_n{}^{T})^{-1} \tag{47}$$

$$\hat{q}_{n+1} = \hat{q}_{n-1} + K_n(d_{n-1} - H_n \hat{q}_{n-1}) \tag{48}$$

where, $\hat{q}_n$ represent the updated estimate of the state, H_n represents the estimated state's measurement model, K_n represents the Kalman gain vector, P_n refers to the prediction error's covariance, R_n is the covariance matrix of v_n, and M_n represent the covariance matrices of v_n. The system's partial derivative as per the MF's weight is evaluated as shown below [15].

$$\frac{\partial s}{\partial w_{ij}} = \frac{\partial s}{\partial u_{fa}} \times \frac{\partial u_{fa}}{\partial f} \times \frac{\partial f}{\partial w_{ij}} \tag{49}$$

where,

$$\frac{\partial s}{\partial u_{fa}} = \frac{s(t) - s(t-1)}{u_{fa}(t) - u_{fa}(t-1)},$$

$$\frac{\partial u_{fa}}{\partial f} = -(G^T B)^{-1} k_o |s(t)|^{\beta(s,\dot{s})} (3 - 4(f(s,\dot{s}))^2)(f(s,\dot{s}))^2,$$

$$\frac{\partial f}{\partial w_{ij}} = \frac{\mu_{ij}}{\sum_{i=1}^{7}\sum_{j=1}^{7} \mu_{ij}}.$$

The partial derivative of the system output for fuzzy MF centers is computed by using the following chain

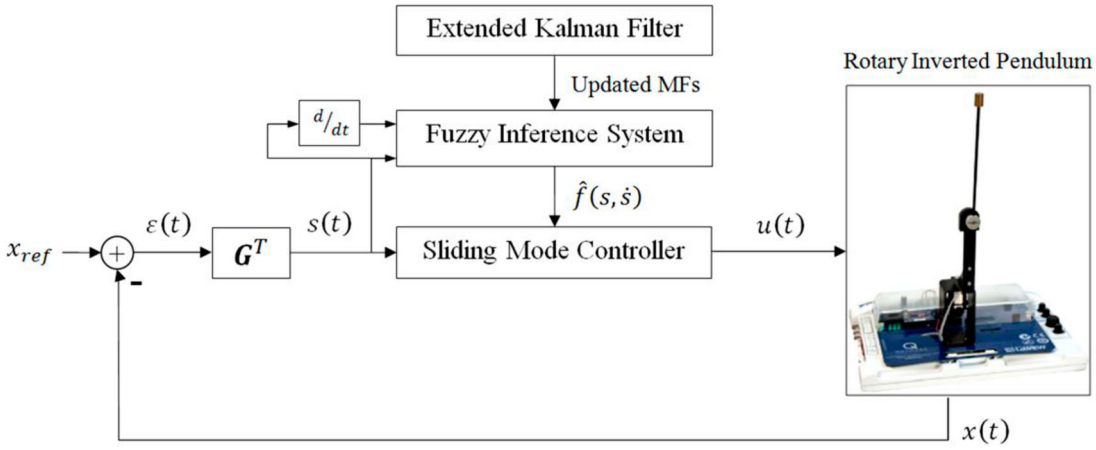

Figure 3. Block diagram of the proposed SFA-SMC.

rule [15].

$$\frac{\partial s}{\partial c_{ij}} = \frac{\partial s}{\partial u_{fa}} \times \frac{\partial u_{fa}}{\partial f} \times \frac{\partial f}{\partial \mu_{i,j}} \times \frac{\partial \mu_{i,j}}{\partial c_{ij}} \tag{50}$$

where,

$$\frac{\partial f}{\partial \mu_{i,j}} = \frac{\sum_{m=1}^{7}\sum_{n=1}^{7}\mu_{mn}(w_{ij}-w_{mn})}{\left(\sum_{m=1}^{7}\sum_{n=1}^{7}\mu_{mn}\right)^2},$$

$$\frac{\partial \mu_{i,j}}{\partial c_{ij}} = \begin{cases} -\frac{1}{b_{ij}^{-}}, & -b_{ij}^{-} \le x - c_{ij} \le 0 \\ \frac{1}{b_{ij}^{+}}, & 0 \le x - c_{ij} \le b_{ij}^{+} \\ 0, & \text{otherwise} \end{cases}.$$

The partial derivative of the MF's right and left half-widths is computed, as shown below [15].

$$\frac{\partial s}{\partial b_{ij}^{-/+}} = \frac{\partial s}{\partial u} \times \frac{\partial u}{\partial f} \times \frac{\partial f}{\partial \mu_{i,j}} \times \frac{\partial \mu_{i,j}}{\partial b_{ij}^{-/+}} \tag{51}$$

where,

$$\frac{\partial \mu_{i,j}}{\partial b_{ij}^{-/+}} = \begin{cases} -\frac{x-c_{ij}}{(b_{ij}^{-})^2}, & -b_{ij}^{-} \le x - c_{ij} \le 0 \\ \frac{x-c_{ij}}{(b_{ij}^{+})^2}, & 0 \le x - c_{ij} \le b_{ij}^{+} \\ 0, & \text{otherwise} \end{cases}$$

The augmentation of the FA-SMC law with EKF yields the Self-Regulating FA-SMC (or SFA-SMC) law presented in Eq. 52.

$$u_s(t) = -(G^T B)^{-1}(G^T A x(t) + \hat{k}(s,\dot{s})|s(t)|^{\hat{\beta}(s,\dot{s})}\hat{f}(s,\dot{s})) \tag{52}$$

The asymptotic stability proof and the finite-time convergence analysis prescribed for the SMC law in Section 2.2 are also valid for the proposed SFA-SMC law. The proposed augmentation further increases the controller's agility to flexibly reconfigure the applied control force. The SFA-SMC is shown in Figure 3.

5. Results and discussions

This section discusses the specifics of the hardware configuration and the experiments used to assess the efficacy of the aforementioned controllers.

5.1. Hardware platform

In this research, the Quanser single-link RIP setup is used as the benchmark platform to carry out the HIL experiments. The Quanser RIP setup used to conduct experiments is shown in Figure 4. The state measurements related to θ and α are acquired via their respective rotary encoders. These NI-ELVIS II data acquisition board is used to acquire samples of raw state measurements at a rate of 1.0 kHz. Upon digitization, the measurement data is transmitted serially at 9600 bps to a customized control application in LABVIEW.

The software's "Block Diagram" tool and functions palette are used to create the control application. A 2.0 GHz laptop with 8.0 GB of RAM is used to run the said control program. Apart from using the built-in functions, libraries, and blocks, the algebraic equations are realized by programming them using C-language code. The control program re-calibrates the function $\hat{f}(s,\dot{s})$ online as per the updated state measurements and makes the necessary parameter adjustments to produce the new control signal. The onboard motor driver circuit receives the control signals serially that are amplified to activate the DC servo motor. The graphical user interface of this control application serves to display and record (download) the real-time variations in the states and control requirements of the RIP system.

5.2. Experimental evaluation

The RIP system's balance control performance under the control of the LQR, SMC, FA-SMC, and SFA-SMC schemes is individually investigated via five specific test cases that emulate practical disturbance conditions. In each test case, the time-domain profiles of $\theta(t)$, $\dot{\theta}(t)$,

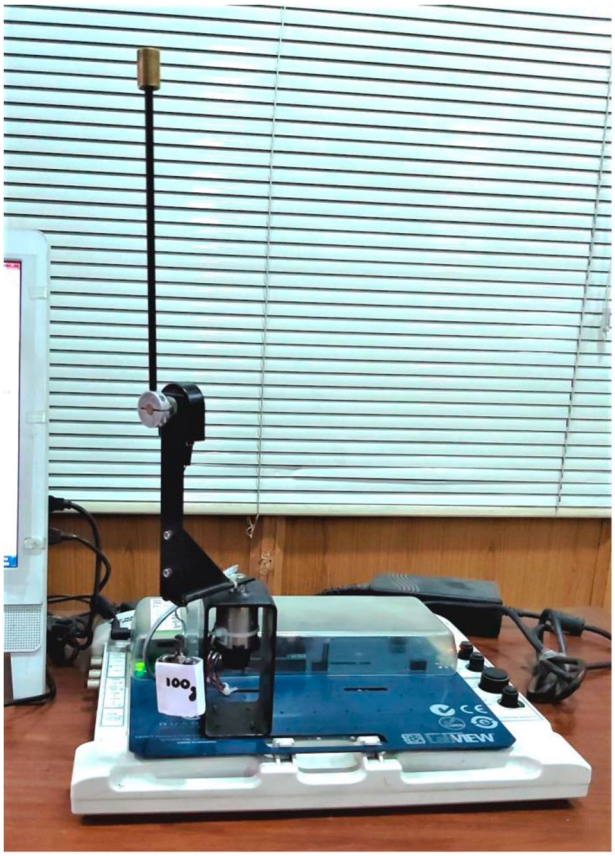

Figure 4. The QNET Rotary Inverted Pendulum setup.

$\alpha(t)$, $\dot{\alpha}(t)$, $V_m(t)$, and $f(s, \dot{s})$ are visualized for analysis. The testing procedures and the corresponding results are presented below:

(A) ***Reference-tracking:*** This experiment examines the pendulum rod's position regulation and arm's station-keeping behavior under no-disturbance conditions. The state responses, control input response, and the variations in $f(.)$ are illustrated in Figure 5.

(B) ***Impulse disturbance compensation:*** This experiment analyzes the controller's sturdiness against the exogenous impulsive disturbances by applying a simulated signal, having a peak of -5.0 V and a span of 100.0 ms, to the $V_m(t)$ signal. The disturbances are injected whenever the arm displaces to its local maximum position. The variations in the states, control input, and $f(.)$ are depicted in Figure 6.

(C) ***Step perturbation compensation:*** This test examines the resistance of the control laws against abrupt and constant load or exogenous torque variations. The disturbance scenario is simulated by administering a step signal of -5.0 V in $V_m(t)$ signal at $t \approx 7.0$ s mark. The consequent variations in the states, control input, and $f(.)$ are demonstrated in Figure 7.

(D) ***Sinusoidal perturbation attenuation:*** This test case examines each controller's agility against the disturbances contributed by mechanical perturbations or air resistance. The experiment is performed by applying a simulated sinusoidal signal, $d(t) = 1.5\sin(20\pi t)$, in the $V_m(t)$ signal. The changes in the states, control input, and $f(.)$ are depicted in Figure 8.

(E) ***Model error compensation:*** This experiment investigates the flexibility of each control law to effectively suppress the perturbations caused by parametric variations, identification errors, or model changes in the RIP system. The experiment is carried out by suspending a 0.10 kg mass underneath the horizontal link of the arm at $t \approx 7.0$ s as shown in Figure 4. This attachment permanently modifies the constituents of the matrix $\boldsymbol{A}$ and, hence, the system's model. The contradiction in the system's updated and reference mathematical model perturbs the pendulum's state and control responses. The resulting variations in the states, control input, and $f(.)$ are illustrated in Figure 9.

(F) ***Gaussian noise attenuation:*** This test case examines each controller's agility against the measurement noise contributed by the sensors. The experiment is conducted by applying a simulated white Gaussian noise signal having a mean of zero and variance of 0.2 in the $V_m(t)$ signal. The changes in the states, control input, and $f(.)$ are depicted in Figure 10.

5.3. Results and discussions

The following key performance metrics (KPMs) are used to analyze the experimental outcomes:

- $E_{x,rms}$: State error's root mean squared (RMS) value.
- $T_{s,\theta}$: Recovery duration for the apparatus rod following an impulse disturbance.
- $|OS_\theta|$: Absolute value of post-disturbance overshoot (or undershoot) observed in the rod.
- E_{offset}: Offset in the arm position following a step disturbance.
- α_{pp}: Peak-to-peak oscillation amplitude observed in the arm after step disturbance.
- V_{ms}: Motor voltage's mean-squared value.
- V_{p}: Peak motor voltage generated following an external disturbance.
- S_θ: RMS value of sensitivity that is evaluated as the ratio of $\Delta\theta$ to ΔV_m.

The performance metrics described above are used in this article to analyze the RIP's disturbance attenuation ability, position regulation accuracy, and control efficiency in the physical environment [47]. The results of the HIL experiments are quantified in Table 3.

In **Experiment A**, the LQR exhibits poor position regulation accuracy and economic control activity.

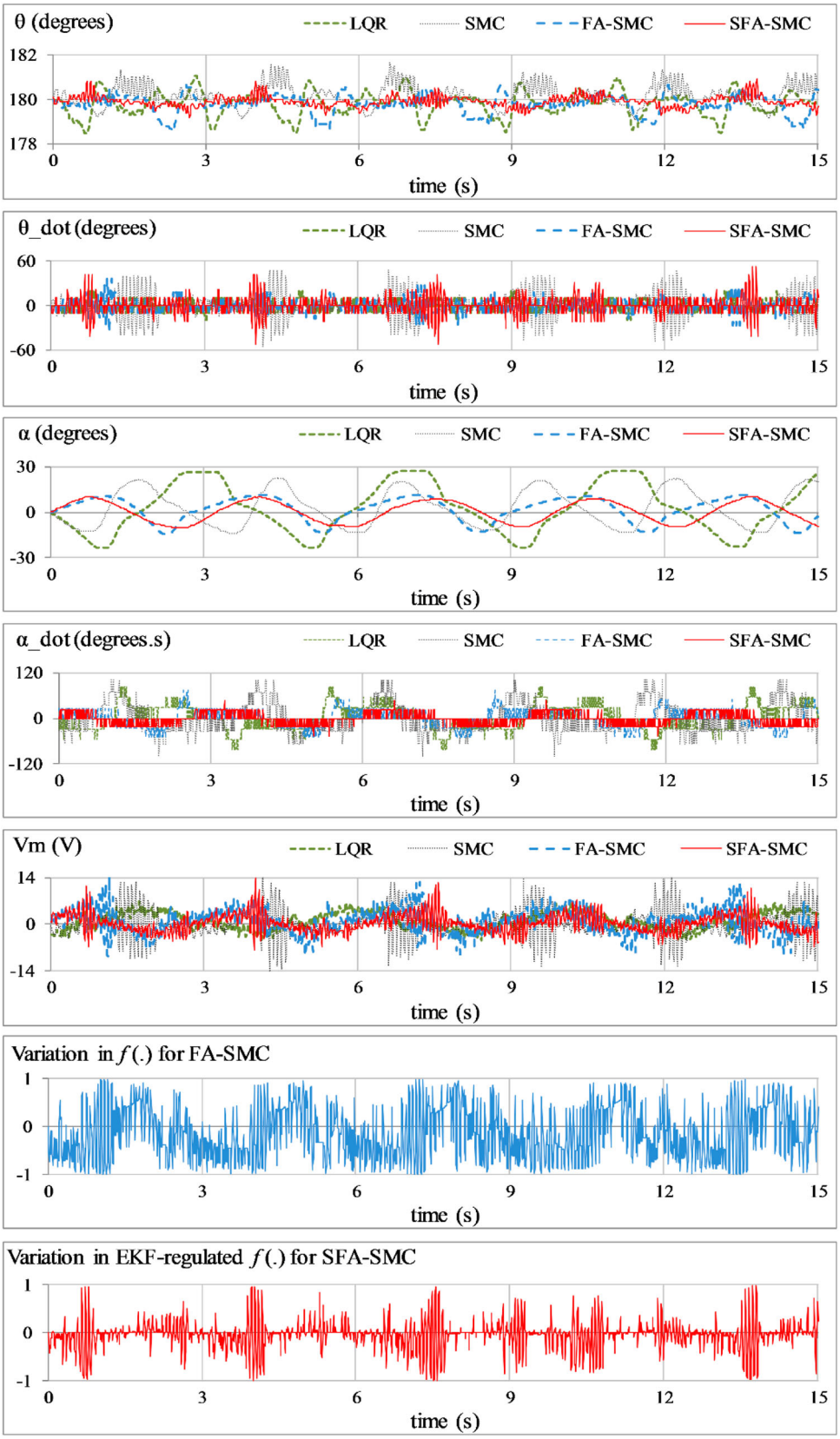

Figure 5. RIP's response under normal conditions.

The SMC-regulated system demonstrates deficient reference-tracking activity with large state fluctuations, high chattering content, and highly disrupted control activity. The FA-SMC demonstrates moderately improved position-regulation behavior with relatively less chattering and fluctuations. However, it imposes large control requirements on the actuator. The SFA-SMC surpasses the other controller variants by robustly minimizing position-regulation errors while economizing the overall control input requirements, which significantly suppresses the chattering content

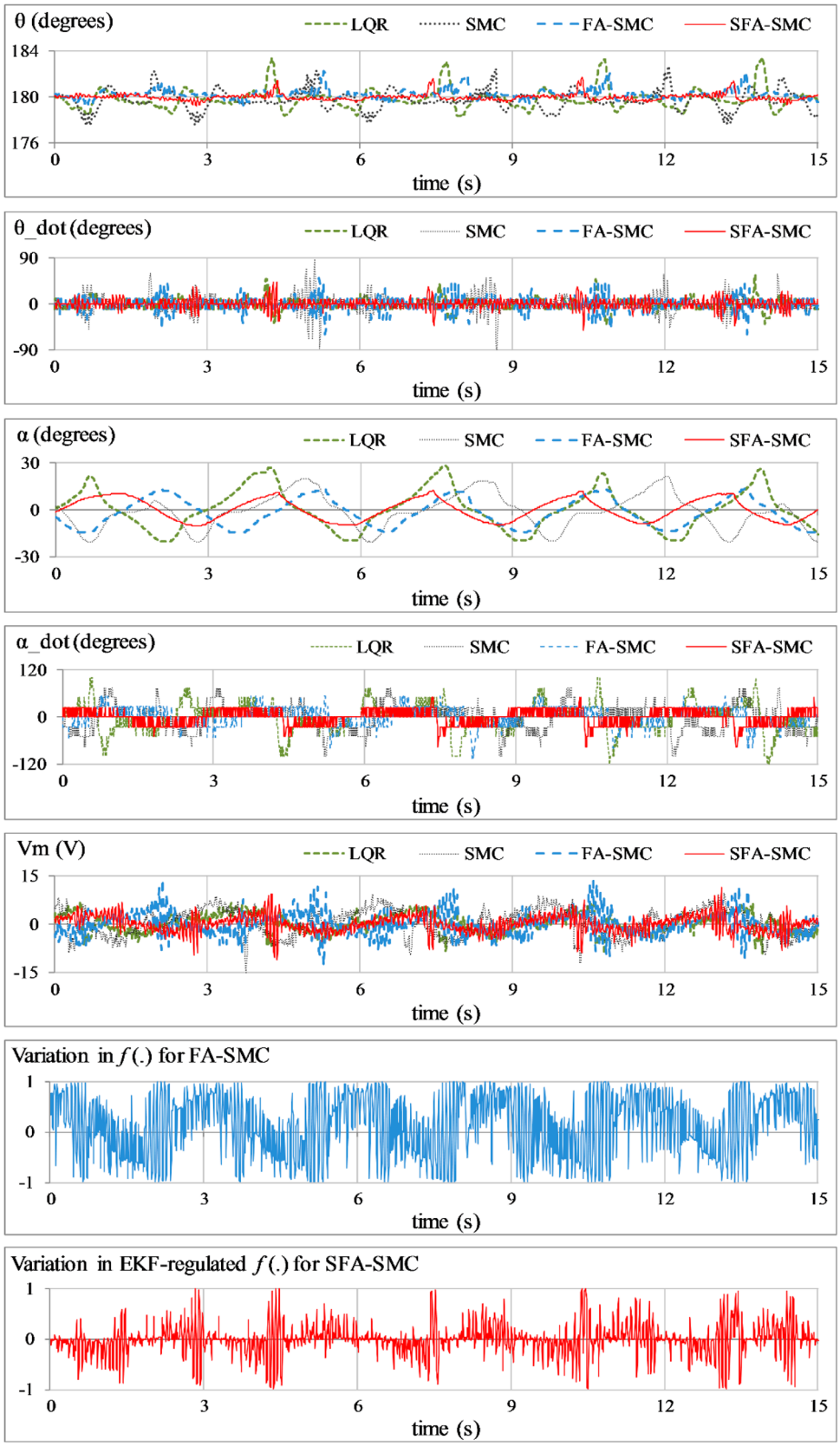

Figure 6. RIP's response under impulsive disturbances.

as well. In **Experiment B**, the LQR demonstrates deficient disturbance-rejection behavior. The SMC demonstrates a mediocre improvement as compared to LQR. However, it still exhibits slow transits with fragile control effort against the simulated disturbance signals, significant chattering content in the responses, and the imposition of peak servo demands upon the actuator. The FA-SMC exhibits reasonably improved damping against disturbances and chattering but displays

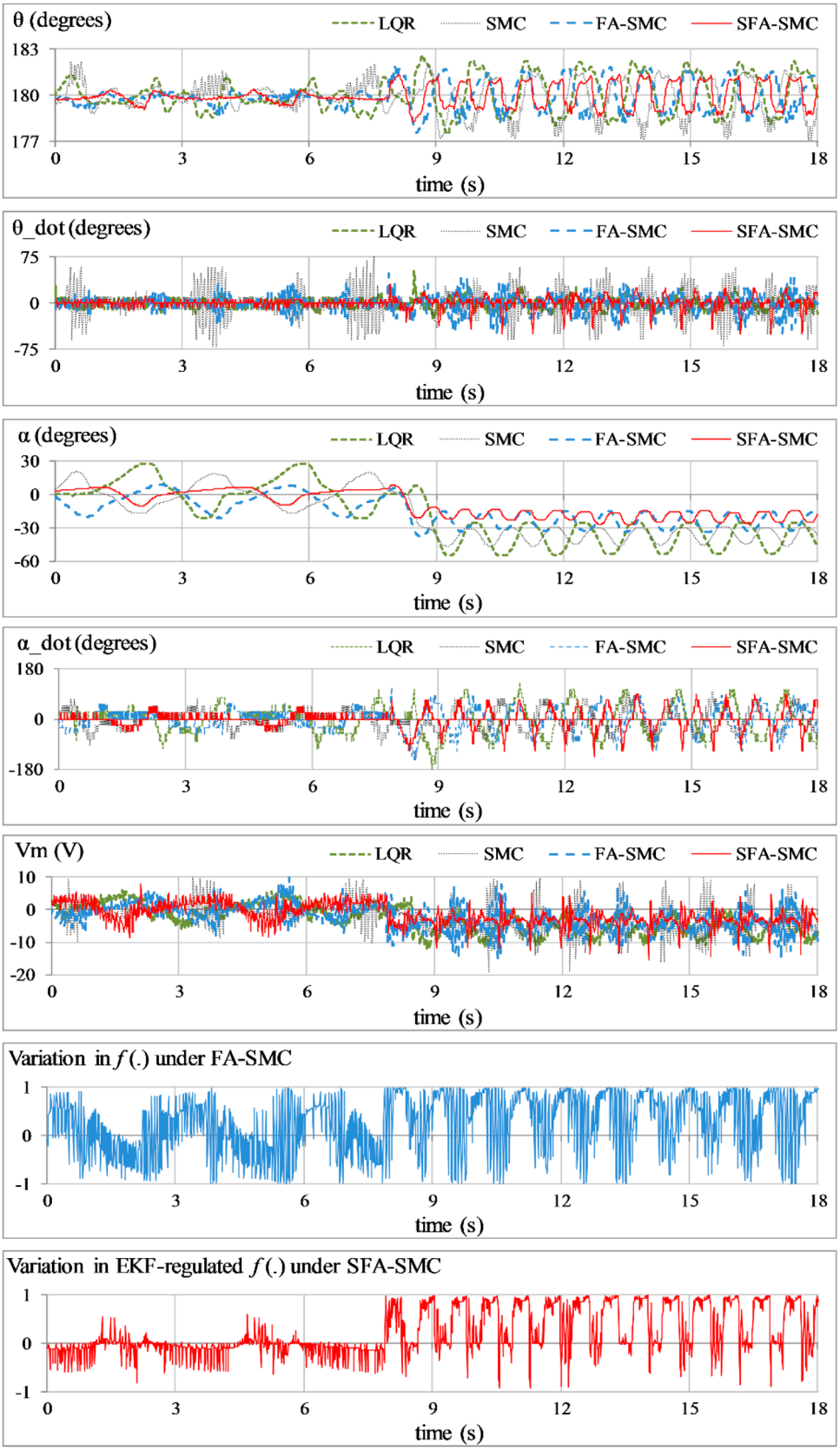

Figure 7. RIP's response under step disturbances.

mediocre control performance. The SFA-SMC significantly enhances the disturbance-rejection capability by exhibiting a relatively faster response speed with a robust control effort to mitigate the overshoots while effectively cutting down the control energy requirements and, thus, the chattering content. In **Experiment C**, the LQR exhibits the poorest disturbance compensation behavior. The SMC continues to display poor disturbance-compensation activity by recording the largest magnitude in offset and α_{pp} in the

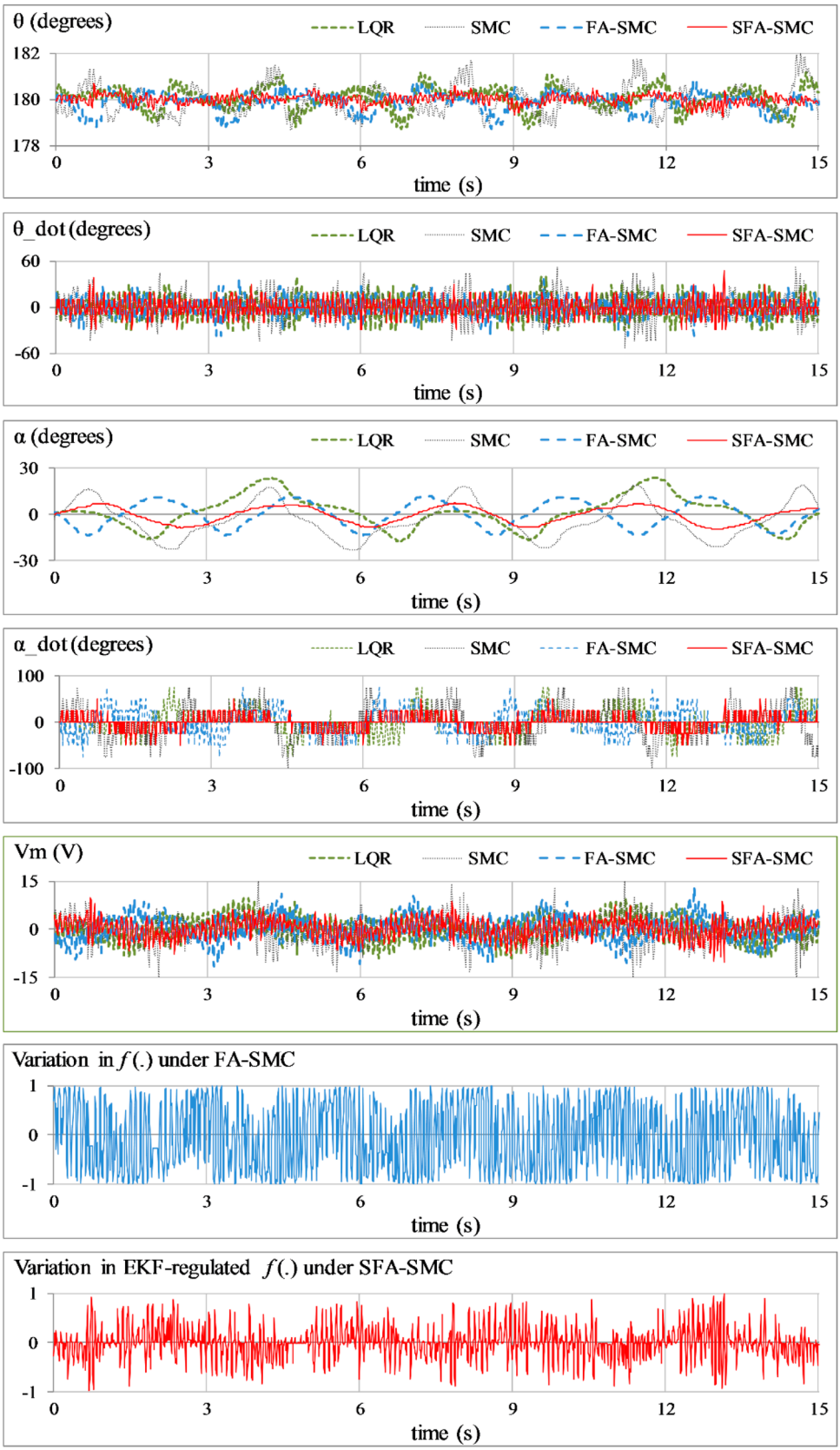

Figure 8. RIP's response under sinusoidal disturbances.

pendulum's observed states and highly disrupted control activity. The FA-SMC shows considerable enhancement in the closed-loop system's control input activity and disturbance attenuation ability. The SFA-SMC contributes the strongest disturbance-rejection behavior by exhibiting minimal offset and α_{pp} in the arm. It also ensures a smooth and economical control activity with minimal peaks recorded. In **Experiment D**, the LQR yields insufficient control effort. The SMC yields an exceedingly disrupted control behavior,

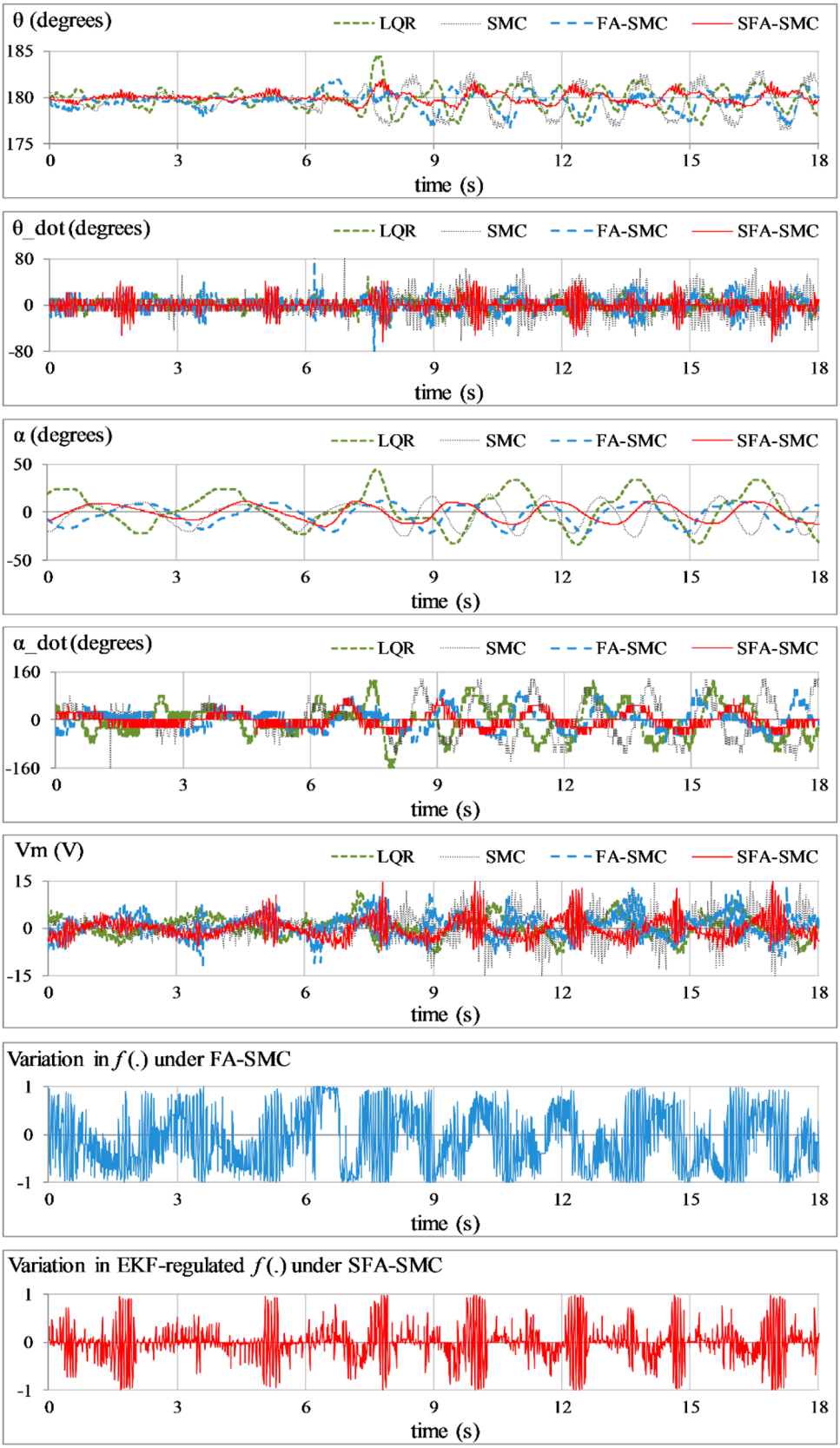

Figure 9. RIP's response under model variation.

which unavoidably introduces high chattering content in the states. The FA-SMC shows considerable improvement in the lumped disturbance attenuation behavior while moderately economizing the control energy demands. The SFA-SMC efficiently attenuates the impact of the simulated sinusoidal disturbance by minimizing steady-state fluctuations and curbing the input requirements. In **Experiment E**, the SMC and FA-SMC contribute relatively weak damping control efforts against the modeling error, which results in large

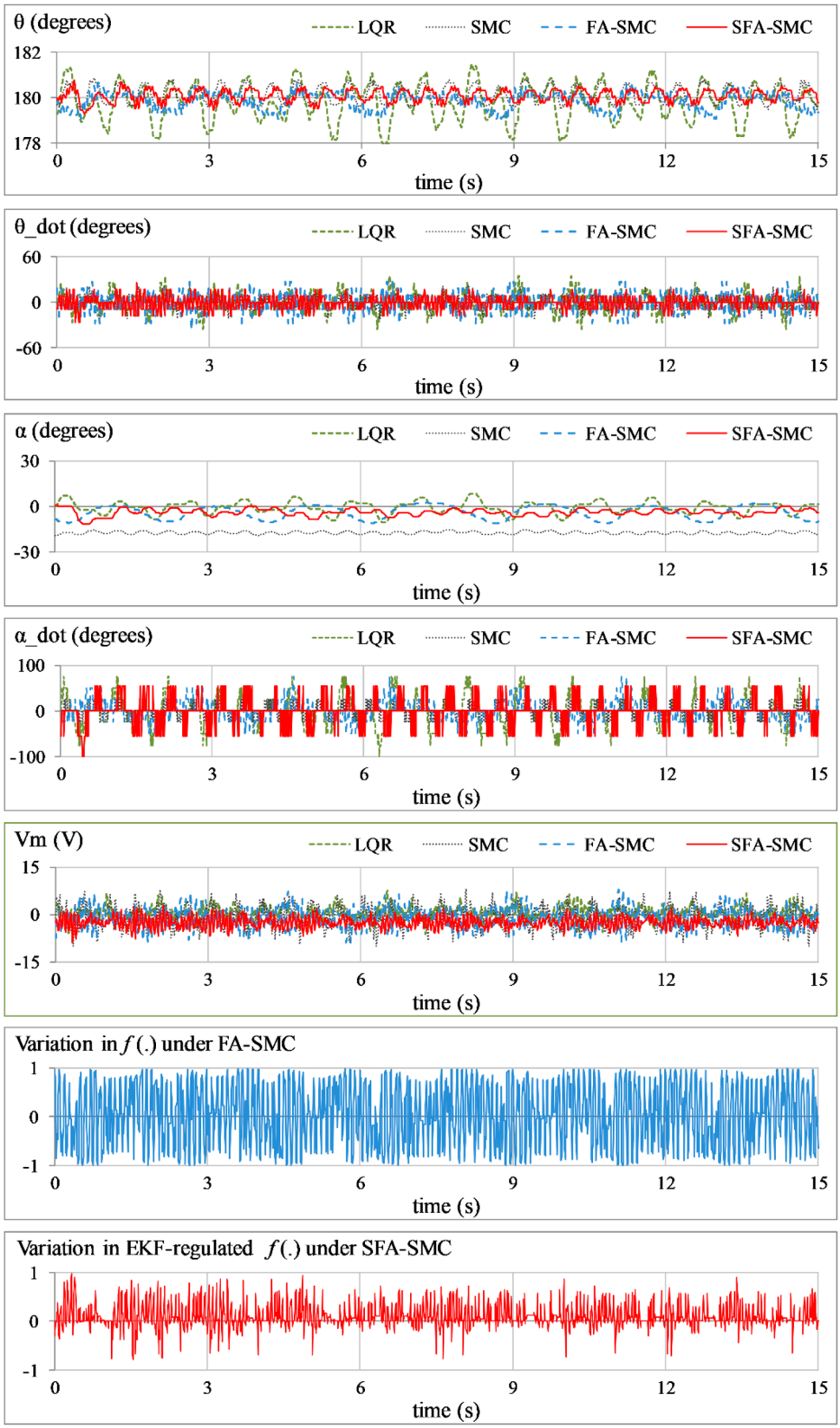

Figure 10. RIP's response under Gaussian white noise.

state fluctuations. The SFA-SMC strongly rejects the impact of the modeling error by effectively attenuating the ensuing state fluctuations, suppressing the chatter, and ensuring an inexpensive energy expenditure. The comparative performance study attests to the SFA-SMC's better position regulation accuracy, stronger disturbance attenuation ability, quicker response time, and improved control effectiveness in all of the HIL experiments.

In **Experiment F**, the LQR underperforms as compared to the rest of the designed controllers. The SMC yields a discontinuous control effort, which

Table 3. Quantitative summary of experimental findings.

	KPM		Control Scheme			
Experiment	Symbol	Unit	LQR	SMC	FA-SMC	SFA-SMC
A	$E_{\text{rms},\theta}$	degrees	0.58	0.56	0.47	0.28
	$E_{\text{rms},\alpha}$	degrees	16.95	12.22	8.03	6.62
	V_{ms}	V^2	7.04	15.81	13.20	8.14
	S_θ	degrees/V	0.87	1.31	1.09	0.48
B	$E_{\text{rms},\theta}$	degrees	0.84	0.87	0.49	0.30
	$\lvert OS_\theta \rvert$	degrees	3.48	2.61	2.28	1.70
	$T_{s,\theta}$	sec.	0.80	0.76	0.39	0.21
	$E_{\text{rms},\alpha}$	degrees	12.56	10.83	9.01	6.81
	V_{ms}	V^2	7.79	17.88	13.54	7.66
	V_{p}	V	−9.19	−15.62	−12.82	−11.09
	S_θ	degrees/V	0.88	2.78	0.79	0.45
C	$E_{\text{rms},\theta}$	degrees	1.19	1.11	0.90	0.71
	$E_{\text{rms},\alpha}$	degrees	31.47	27.93	19.95	14.65
	E_{offset}	degrees	−38.65	−36.62	−24.28	−19.98
	α_{pp}	degrees	25.20	23.77	20.41	15.08
	V_{ms}	V^2	26.27	21.88	17.88	14.22
	V_{p}	V	−12.05	−19.30	−15.41	−15.35
	S_θ	degrees/V	2.55	5.14	1.51	0.76
D	$E_{\text{rms},\theta}$	degrees	1.19	0.61	0.42	0.21
	$E_{\text{rms},\alpha}$	degrees	18.07	12.15	8.09	5.18
	V_{ms}	V^2	11.41	17.30	14.39	8.81
	S_θ	degrees/V	2.26	0.67	0.54	0.51
E	$E_{\text{rms},\theta}$	degrees	0.51	1.47	0.98	0.61
	$E_{\text{rms},\alpha}$	degrees	9.94	13.42	10.81	8.01
	V_{ms}	V^2	12.27	16.54	13.81	10.03
	S_θ	degrees/V	2.42	3.69	1.52	1.28
F	$E_{\text{rms},\theta}$	degrees	0.82	0.43	0.39	0.28
	$E_{\text{rms},\alpha}$	degrees	9.94	7.30	5.91	4.42
	V_{ms}	V^2	12.27	11.34	10.66	9.18
	S_θ	degrees/V	2.21	0.62	0.51	0.49

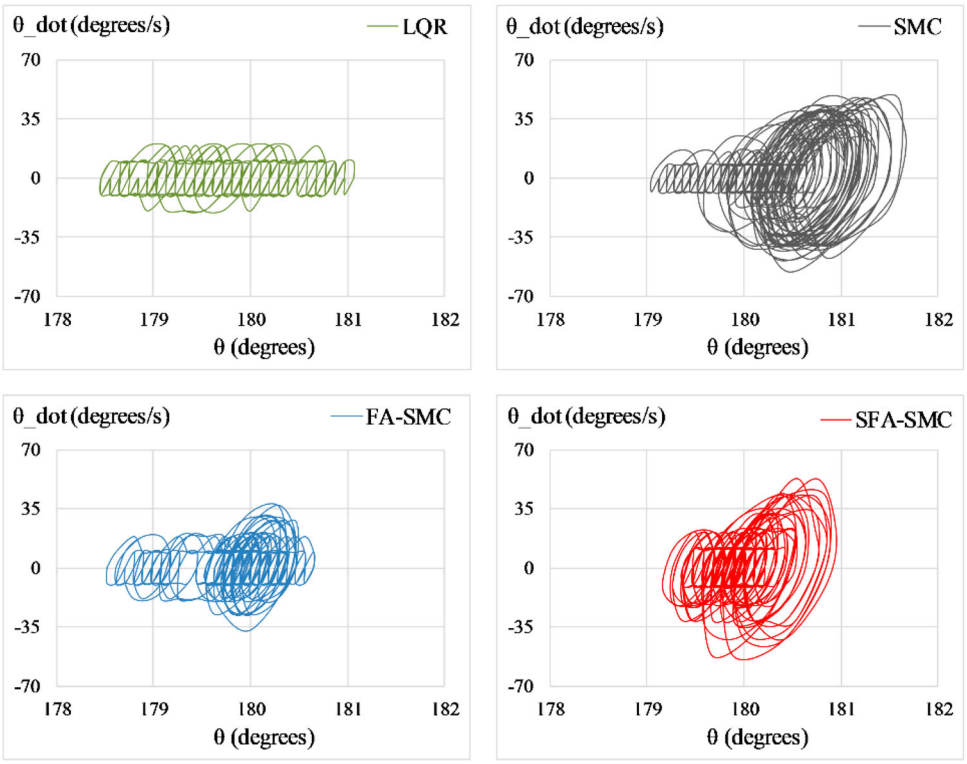

Figure 11. Phase portrait between $\dot{\theta}(t)$ and $\theta(t)$ for each control law.

inevitably introduces large ripples in state responses. The FA-SMC shows considerable improvement in white noise suppression behavior while expending a reasonable amount of control energy. The SFA-SMC robustly attenuates the white noise by minimizing the oscillations in the state responses as well as the control energy requirements.

The benefits afforded by SFA-SMC are attributed to the dynamic reconfiguration of the shape and form of $f(s, \dot{s})$. In every test case, the variations in $f(s, \dot{s})$ under

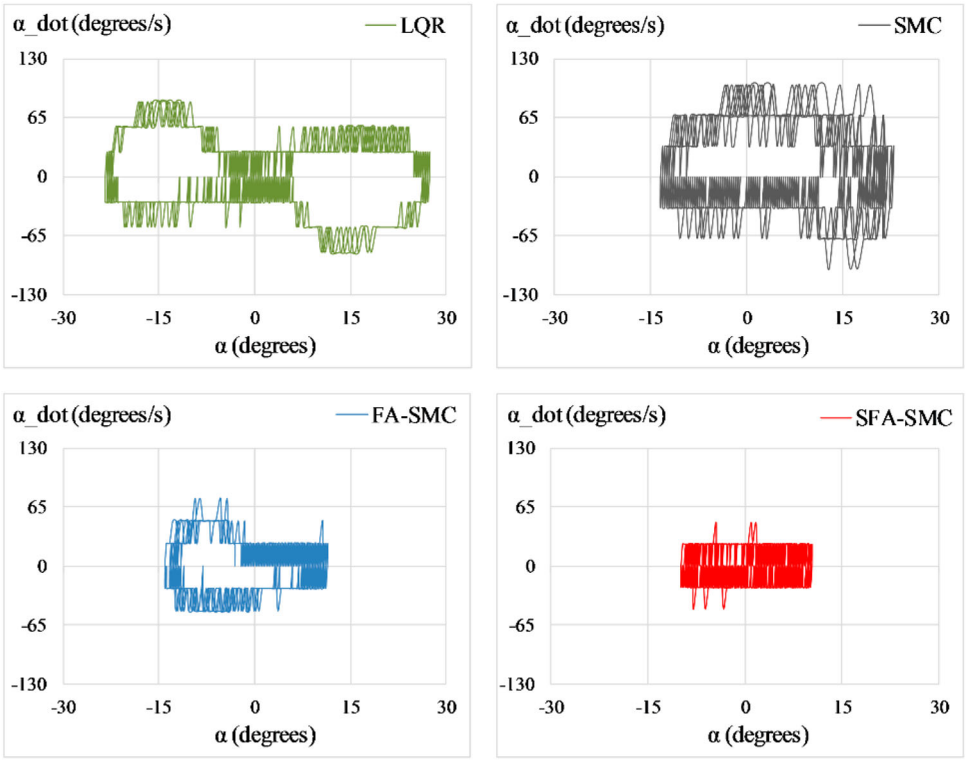

Figure 12. Phase portrait between $\dot{\alpha}(t)$ and $\alpha(t)$ for each control law.

Table 4. Comparison of SFA-SMC with state-of-the-art controllers.

	KPM		Control Scheme			
Experiment	Symbol	Unit	CFO-LQIR [21]	IVS-LQIC [22]	IDoS-LQR [23]	SFA-SMC (Proposed)
A	$E_{\text{rms},\theta}$	degrees	0.36	0.35	0.29	**0.28**
	$E_{\text{rms},\alpha}$	degrees	10.08	8.52	9.28	**6.62**
	V_{ms}	V^2	7.18	**7.06**	7.08	8.14
B	$E_{\text{rms},\theta}$	degrees	0.47	0.35	0.37	**0.30**
	$\lvert OS_\theta \rvert$	degrees	2.23	1.68	**1.47**	1.70
	$T_{s,\theta}$	sec.	0.51	0.46	0.46	**0.21**
	$E_{\text{rms},\alpha}$	degrees	9.68	8.74	8.92	**6.81**
	V_{ms}	V^2	6.39	7.74	**6.31**	7.66
	V_{p}	V	−8.47	−9.55	**−8.13**	−11.09
C	$E_{\text{rms},\theta}$	degrees	**0.42**	0.59	0.45	0.71
	$E_{\text{rms},\alpha}$	degrees	22.06	16.62	17.43	**14.65**
	E_{offset}	degrees	−23.72	**−19.08**	−23.00	−19.98
	α_{pp}	degrees	21.61	20.70	18.65	**15.08**
	V_{ms}	V^2	25.35	22.76	18.10	**14.22**
	V_{p}	V	**−10.34**	−11.22	−12.28	−15.35
D	$E_{\text{rms},\theta}$	degrees	0.29	0.27	0.29	**0.21**
	$E_{\text{rms},\alpha}$	degrees	9.53	5.58	6.85	**5.18**
	V_{ms}	V^2	10.50	9.59	9.07	**8.81**
E	$E_{\text{rms},\theta}$	degrees	0.78	0.63	0.75	**0.61**
	$E_{\text{rms},\alpha}$	degrees	11.78	9.56	9.94	**8.01**
	V_{ms}	V^2	9.48	11.04	**8.49**	10.03

Note: Bold values indicate the optimum value of a given performance metric yielded by the designed controllers.

FA-SMC are relatively more disrupted. The function is redundantly and abruptly switching between +1 and −1, which inevitably results in a very sporadic control action and the consequent chattering phenomenon. On the contrary, the variations in the EKF-regulated $\hat{f}(s, \dot{s})$ under SFA-SMC are smooth. The functional variations are abrupt, but they only commute to +1 and −1 under large error conditions. The variations are mostly condensed around the intermediate values of the function under normal conditions. This behavior economizes the system's control input requirements, which leads to smooth control activity and reduces chattering. The SFA-SMC avoids the inherent shortcomings of the conventional fuzzy system by employing EKF to dynamically reconfigure the MFs, which in turn supplements the controller's self-tuning capability in real time. The sensitivity analysis quantified in Table 3 also validates the superior robustness of SFA-SMC to disturbances and noise.

The phase diagrams for test case A, plotted between the angular velocity and angular displacement associated with the arm and the pendulum rod, are depicted

visually in Figure 11 and Figure 12, respectively. The phase portraits linked with θ show that the state variations in SFA-SMC are restricted within −179.0 and 181.0 degrees while exhibiting relatively high response speed. The phase portraits linked with α show that the state variations in SFA-SMC are restricted within −14.0 and 14.0 degrees while exhibiting reasonable response speed. The phase diagrams validate the agility of the proposed SFA-SMC law.

5.4. Comparative analysis using modern controllers

The proposed SFA-SMC is also benchmarked against state-of-the-art controllers to verify its robustness in addressing the RIP's balancing control problem. The state-of-the-art control schemes considered for the sake of comparison are the Complex-Fractional-Order Linear-Quadratic-Integral-Regulator (CFO-LQIR) [21], Improved Variable-Structure Linear-Quadratic-Integral-Controller (IVS-LQIC) [22], and Immune-Adaptive Degree-of-Stability LQR (IDoS-LQR) [23]. The aforementioned controllers were experimentally analyzed on the same RIP system, as modeled in Table 1, via test cases (A to E) under the same operating conditions. This arrangement ensures a fair comparison.

The graphical visualization of the experimental results associated with the aforementioned (selected) control schemes is clearly illustrated in the articles [21–23] respectively. The comparative performance analysis is presented in Table 4, which justifies that the disturbance compensation, position regulation behavior, time optimality, and chattering suppression of the proposed SFA-SMC are on par with modern controllers. Most of the KPMs associated with the SFA-SMC surpass the respective KPMs of other controllers, as quantified (and highlighted) in Table 4.

6. Conclusion

This study discusses the methodical development and experimental verification of a novel self-tuning SMC procedure that undertakes to strengthen the disturbance attenuation ability of an RIP system while simultaneously minimizing the chattering in the response as well as the control energy expenditure. For this purpose, the SMC is methodically modified by retrofitting it with auxiliary adaptation tools. The proposed augmentations increase the controller's durability against external disturbances and suppress the chattering while upholding the closed-loop stability of the RIP system. The EKF-driven dynamic reconfiguration of the fuzzy nonlinear function's waveform to self-adjust the critical controller parameters significantly improves the controller's agility to achieve the desired objectives. Consequently, the system exhibits minimum transitional times while effectively attenuating the disturbance-induced overshoots (and oscillations) and economically managing the control input demands. The experimental findings successfully validate the enhanced self-balancing behavior of the SFA-SMC in the physical environment. In the future, the SFA-SMC law can be appropriately modified and extended to other electro-mechanical and energy-conversion systems as well. Furthermore, apart from exogenous disturbances, the proposed augmentations can be retrofitted with other variants of SMC laws to address hardware limits and parametric uncertainties. Finally, a rigorous experimental comparison must be done to benchmark the efficacies of the SFA-SMC law against the ubiquitous disturbance-observer-based SMC laws.

Disclosure statement

No potential conflict of interest was reported by the author(s).

Funding

The authors would like to acknowledge the support of the deanship of scientific research at Najran University, Ministry of Education, Kingdom of Saudi Arabia for this research through a grant (NU/ RG/SERC/12/29) under the Funding Committee of the deanship of scientific research at Najran University, Kingdom of Saudi Arabia.

ORCID

Arslan Ahmed Amin http://orcid.org/0000-0001-8035-595X

References

[1] Dalvand MM, Shirinzadeh B, Nahavandi S. Swing-up and stability control of wheeled acrobot (WAcrobot). Automatika. 2014;55(1):32–40. doi:10.7305/automatika.2014.01.109

[2] Boubaker O, Iriarte R. The inverted pendulum in control theory and robotics: from theory to new innovations. Stevenage: Institution of Engineering and Technology; 2017.

[3] Saleem O, Mahmood-ul-Hasan K. Robust stabilisation of rotary inverted pendulum using intelligently optimised nonlinear self-adaptive dual fractional-order PD controllers. Int J Syst Sci. 2019;50:1399–1414. doi:10.1080/00207721.2019.1615575

[4] Abdullah M, Amin AA, Iqbal S, et al. Swing Up and stabilization control of rotary inverted pendulum based on energy balance, fuzzy logic, and LQR controllers. Meas Control. 2021;54:1356–1370. doi:10.1177/00202940211035406

[5] Majumder K, Patre BM. Adaptive sliding mode control for asymptotic stabilization of underactuated mechanical systems via higher-order nonlinear disturbance observer. J Vib Control. 2019;25:2340–2350. doi:10.1177/1077546319853199

[6] Saleem O, Rizwan M, Awan FG. Robustification of the state-space MRAC Law for under-actuated systems via fuzzy-immunological computations. Sci Progress. 2022;105:003685042211222. doi:10.1177/00368504221122291

[7] Saleem O, Rizwan M, Mahmood-ul-Hasan K, et al. Performance enhancement of multivariable model reference optimal adaptive motor speed controller using error-dependent hyperbolic gain functions. Auto matika. 2020;61(1):117–131. doi:10.1080/00051144.2019.1688508
[8] Szuster M, Hendzel Z. Intelligent optimal adaptive control for mechatronic systems. Springer, Cham; 2017.
[9] Krafes S, Chalh Z, Saka A. A review on the control of second order underactuated mechanical systems. *Complexity* 2018;2018:9573514. doi:10.1155/2018/9573514
[10] Saleem O, Mahmood-ul-Hasan K, Rizwan M. An experimental comparison of different hierarchical self-tuning regulatory control procedures for under-actuated mechatronic systems. PLoS One. 2021;16:e0256750.
[11] Bhatti OS, Mehmood-ul-Hasan K, Imtiaz MA. Attitude control and stabilization of a Two-wheeled self-balancing robot. Control Eng Appl Inform. 2015;17:98–104.
[12] Tabatabaei M, Barati-Boldaji R. Non-overshooting PD and PID controllers design. Automatika. 2017;58(4):400–409. doi:10.1080/00051144.2018.1471824
[13] Naz F, Wajid Z, Amin AA, et al. Pid tuning with reference tracking and plant uncertainty along with disturbance rejection. Syst Sci Control Eng. 2021;9:160–166. doi:10.1080/21642583.2021.1888817
[14] Saleem O, Rizwan M, Zeb AA, et al. Online adaptive PID tracking control of an aero-pendulum using PSO-scaled fuzzy gain adjustment mechanism. Soft Comput. 2020;24:10629–10643. doi:10.1007/s00500-019-04568-1
[15] Bhatti OS, Tariq OB, Manzar A, et al. Adaptive intelligent cascade control of a ball-riding robot for optimal balancing and station-keeping. Adv Robot. 2018;32:63–76. doi:10.1080/01691864.2017.1399825
[16] Ramya A, Imthiaz A, Balaji M. Hybrid self tuned fuzzy PID controller for speed control of brushless DC motor. Automatika. 2016;57(3):672–679. doi:10.7305/automatika.2017.02.1769
[17] Bekkar B, Ferkous K. Design of online fuzzy tuning LQR controller applied to rotary single inverted pendulum: experimental validation. Arab J Sci Eng. 2022;48:6957–6972. doi:10.1007/s13369-022-06921-3
[18] Jia C, Kong D, Du L. Recursive terminal sliding-mode control method for nonlinear system based on double hidden layer fuzzy emotional recurrent neural network. IEEE Access. 2022;10:118012–118023. doi:10.1109/ACCESS.2022.3220800
[19] Saleem O. An enhanced adaptive-LQR procedure for under-actuated systems using relative-rate feedback to dynamically reconfigure the state-weighting-factors. J Vib Control. 2022;29:2316–2331. doi:10.1177/10775463221078654
[20] Saleem O, Rizwan M, Mahmood-ul-Hasan K. Self-tuning state-feedback control of a rotary pendulum system using adjustable degree-of-stability design. Automatika. 2021;62(1):84–97. doi:10.1080/00051144.2020.1864186
[21] Saleem O, Abbas F, Iqbal J. Complex fractional-order LQIR for inverted-pendulum-type robotic mechanisms: design and experimental validation. Mathematics. 2023;11(4):913. doi:10.3390/math11040913
[22] Saleem O, Iqbal J, Afzal MS. A robust variable-structure LQI controller for under-actuated systems via flexible online adaptation of performance-index weights. PLoS One. 2023;18(3):e0283079. doi:10.1371/journal.pone.0283079
[23] Saleem O, Iqbal J. Fuzzy-immune-regulated adaptive degree-of-stability LQR for a self-balancing robotic mechanism: design and HIL realization. IEEE Robot Automat Letters. 2023;8(8):4577–4584. doi:10.1109/LRA.2023.3286176
[24] Shah I, Rehman FU. Smooth higher-order sliding mode control of a class of underactuated mechanical systems. Arab J Sci Eng. 2017;42:5147–5164. doi:10.1007/s13369-017-2617-9
[25] Liu J, et al. Advanced sliding mode control for mechanical systems. Berlin: Springer; 2012.
[26] Coban R. Backstepping integral sliding mode control of an electromechanical system. Automatika. 2017;58(3):266–272. doi:10.1080/00051144.2018.1426263
[27] Riaz U, Tayyeb M, Amin AA. A review of sliding mode control with the perspective of utilization in fault tolerant control. Recent Adv Electric Electron Eng. 2021;14:312–324.
[28] Yiğit I. Model free sliding mode stabilizing control of a real rotary inverted pendulum. J Vib Control. 2017;23:1645–1662. doi:10.1177/1077546315598031
[29] Dao PN, Liu YC. Adaptive reinforcement learning strategy with sliding mode control for unknown and disturbed wheeled inverted pendulum. Int J Control Autom Syst. 2021;19(2):1139–1150. doi:10.1007/s12555-019-0912-9
[30] Dao PN, Nguyen VT, Liu YC. Finite-time convergence for bilateral teleoperation systems with disturbance and time-varying delays. IET Control Theory Appl. 2021;15(13):1736–1748. doi:10.1049/cth2.12155
[31] Kang HS, Lee Y, Hyun CH, et al. Design of sliding-mode control based on fuzzy disturbance observer for minimization of switching gain and chattering. Soft Comput. 2015;19:851–858. doi:10.1007/s00500-014-1412-8
[32] Amin AA, Abdullah M. A comparative study of DC-DC buck, boost, and buck-boost converters with proportional-integral, sliding mode, and fuzzy logic controllers. Recent Adv Electric Electron Eng. 2022;15:1–17.
[33] Jafary Fesharaki A, Tabatabaei M. Adaptive hierarchical fractional-order sliding mode control of an inverted pendulum–cart system. Arab J Sci Eng. 2022;47:13927–13942. doi:10.1007/s13369-022-06613-y
[34] Chaouch DE, Ahmed-Foitih Z, Khelfi MF. A self-tuning fuzzy inference sliding mode control scheme for a class of nonlinear systems. J Vib Control. 2012;18:1494–1505. doi:10.1177/1077546311419177
[35] Wang P, Zhang D, Lu B. Robust fuzzy sliding mode control based on low pass filter for the welding robot with dynamic uncertainty. Ind Robot. 2019;47:111–120. doi:10.1108/IR-04-2019-0074
[36] Balamurugan S, Venkatesh P. Fuzzy sliding-mode control with low pass filter to reduce chattering effect: an experimental validation on Quanser SRIP. Sadhana. 2017;42:1693–1703. doi:10.1007/s12046-017-0722-9
[37] Nguyen NP, Oh H, Kim Y, et al. Fuzzy-Based super-twisting sliding mode stabilization control for under-actuated rotary inverted pendulum systems. IEEE Access. 2020;8:185079–185092. doi:10.1109/ACCESS.2020.3029095
[38] Pham TL, Dao PN. Disturbance observer-based adaptive reinforcement learning for perturbed uncertain surface vessels. ISA Trans. 2022;130:277–292. doi:10.1016/j.isatra.2022.03.027

[39] Zhang J, Chen D, Shen G, et al. Disturbance observer based adaptive fuzzy sliding mode control: A dynamic sliding surface approach. Automatica (Oxf). 2021;129:109606. doi:10.1016/j.automatica.2021.109606

[40] Jian Z, Yongpeng Z. Optimal linear modeling and its applications on swing-up and stabilization control for rotary inverted pendulum. In: Proceedings of the 30th Chinese control conference, Yantai, People's Republic of China; 2011. p. 493–500.

[41] Astom KJ, Apkarian J, Karam P, et al. Student Workbook: Qnet rotary inverted pendulum trainer for NI ELVIS. Ontario: Quanser Inc.; 2011.

[42] Saleem O, Mahmood-ul-Hasan K. Adaptive state-space control of under-actuated systems using error-magnitude dependent self-tuning of cost weighting-factors. Int J Control Autom Syst. 2021;19:931–941. doi:10.1007/s12555-020-0209-z

[43] Soltanpour MR, Khooban MH, Khalghani MR. An optimal and intelligent control strategy for a class of nonlinear systems: adaptive fuzzy sliding mode. J Vib Control. 2016;22:159–175. doi:10.1177/1077546314526920

[44] Hernández-Casañas JJ, Márquez-Vera MA, BD B-H. Characterization and adaptive fuzzy model reference control for a magnetic levitation system. Alexandria Eng J. 2016;55:2597–2607. doi:10.1016/j.aej.2016.04.032

[45] Ahn KK, Truong DQ. Online tuning fuzzy PID controller using robust extended Kalman filter. J Process Control. 2009;19:1011–1023. doi:10.1016/j.jprocont.2009.01.005

[46] Saleem O, Omer U. EKF-based self-regulation of an adaptive nonlinear PI speed controller for a DC motor. Turkish J Elect Eng Comput Sci. 2017;25(5):4131–4141. doi:10.3906/elk-1611-311

[47] Saleem O, Mahmood-Ul-Hasan K. Indirect adaptive state-feedback control of rotary inverted pendulum using self-mutating hyperbolic-functions for online cost variation. IEEE Access. 2020;8:91236–91247.